Eruptive Cycle and Bubble Trap of Strokkur Geyser, Iceland

Eva P. S. Eibl[1] , **Daniel Müller[2]** , **Thomas R. Walter[2]** , **Masoud Allahbakhshi[2]** , **Philippe Jousset[2]** , **Gylfi Páll Hersir[3]**, and **Torsten Dahm[1,2]**

[1]Institute of Geosciences, University of Potsdam, Potsdam, Germany, [2]GFZ German Research Centre for Geosciences, Potsdam, Germany, [3]ISOR, Reykjavik, Iceland

Abstract The eruption frequency of geysers can be studied easily on the surface. However, details of the internal structure including possible water and gas filled chambers feeding eruptions and the driving mechanisms often remain elusive. We used a multidisciplinary network of seismometers, video cameras, water pressure sensors and one tiltmeter to study the eruptive cycle, internal structure, and mechanisms driving the eruptive cycle of Strokkur geyser in June 2018. An eruptive cycle at Strokkur always consists of four phases: (1) Eruption, (2) post-eruptive conduit refilling, (3) gas filling of the bubble trap, and (4) regular bubble collapse at shallow depth in the conduit. For a typical single eruption 19 ± 4 bubble collapses occur in Phase 3 and 8 ± 2 collapses in Phase 4 at a mean spacing of 1.52 ± 0.29 and 24.5 ± 5.9 s, respectively. These collapses release latent heat to the fluid in the bubble trap (Phase 3) and later to the fluid in the conduit (Phase 4). The latter eventually reaches thermodynamic conditions for an eruption. Single to sextuple eruptions have similar spacings between bubble collapses and are likely fed from the same bubble trap at 23.7 ± 4.4 m depth, 13–23 m west of the conduit. However, the duration of the eruption and recharging phase linearly increases likely due to a larger water, gas and heat loss from the system. Our tremor data provides documented evidence for a bubble trap beneath a pool geyser.

Plain Language Summary It is easy to study the eruptions of a geyser on the surface. It is however difficult to study the shape of the geyser at depth and the processes that cause eruptions since we cannot observe them directly. Here, we use seismometers, cameras, pressure sensors and one tiltmeter to study the behavior and area beneath pool geyser Strokkur, Iceland, in June 2018. We find that the geyser always passes through four phases: (i) eruption, (ii) refilling of the conduit with water, (iii) gas accumulation in a bubble trap, and (iv) bubbles leaving the bubble trap regularly to collapse in the conduit at shallow depth. Bubble collapses, heating and gas accumulation in the bubble trap takes place at a mean depth of 23.7 ± 4.4 m, 13–23 m west of the conduit (Phase 3). Phase 4 is characterized by regular bubble collapses at shallow depth in the conduit heating the fluids in the conduit to prepare for an eruption. Single to sextuple eruptions behave similar and are likely fed from the same bubble trap offset from the conduit. However, the eruption and recharging phase persists for longer most likely caused by a larger water, gas and heat loss from the system.

1. Introduction

Worldwide around 1,000 geysers exist (Hurwitz & Shelly, 2017). They exhibit spectacular, jetting eruptions of hot water (Descloizeaux, 1847) and can be subdivided into pool and cone geysers. Pool geysers exhibit a large water-filled pool on the surface (Barth, 1940; Belousov et al., 2013; Munoz-Saez, Manga, et al., 2015; Munoz-Saez, Namiki, & Manga, 2015; Nishimura et al., 2006; Walter et al., 2020) while cone geysers merely form cones (Belousov et al., 2013; Karlstrom et al., 2013; Kieffer, 1984; Namiki et al., 2014; Rudolph et al., 2012). The system is composed of a water-filled conduit heated by vapor. The subsurface conduit configuration required to produce a geyser is not completely understood, but recent works indicate that a laterally offset bubble trap may be an important component (Belousov et al., 2013; Vandemeulebrouck et al., 2013). While the reservoir depth might control the eruption height (Reed et al., 2021), the exact geometry, depth or number of bubble traps is difficult to constrain without comprehensive geophysical surveys.

A small percentage of the geysers worldwide erupt in regular intervals passing from the end of one eruption to the end of the next one through an eruptive cycle (Wang & Manga, 2010). Eruptive cycles of geysers

Table 1
Comparison of Geysers Worldwide With Respect to the Type, Number of Phases in Eruptive Cycle, Eruption Interval, Bubble Trap Number, Depth of the Bubble Trap, and Respective References

	Type	Phase	Mean interval	Trap	Depth	References
Old Faithful, US	Cone	5	65 & 93 min	1	20 m, 20 m SW	Kedar et al. (1998); Kieffer (1984); Vandemeulebrouck et al. (2013); Wu et al. (2017, 2019)
Lone Star, US	Cone	4	3.2 h	1	10 m, offset	Karlstrom et al. (2013); Vandemeulebrouck et al. (2014)
Calistoga Geyser, US	Cone		4.6 min	1?	>42 m	Rudolph et al. (2012)
El Jefe, Chile	Pool	4	132 s	1	5–10 m	Ardid et al. (2019); Munoz-Saez, Manga, et al. (2015)
Vega Rinconada, Chile	Pool		1.5 h	1	10–15 m	Munoz-Saez, Namiki, and Manga (2015)
El Cobreloa, Chile	Cone		13.72 & 4.67 h	1	300 m	Namiki et al. (2014)
Onikobe, Japan	Cone		10 min			Nishimura et al. (2006)
Velikan, Russia	Pool	3–4	5 h	1	Offset	Belousov et al. (2013)
Bol'shoy, Russia	Cone	3–4	1 h	1	Offset	Belousov et al. (2013)
Vanna, Russia	Pool	3–4	Several min	1	Offset	Belousov et al. (2013)
Kovarny, Russia	Cone	3–4	Several min	1	Offset	Belousov et al. (2013)
Great Geysir, Iceland	Pool	4	Irregular			Barth (1940)
Strokkur, Iceland	Pool	4	3.7, 6.2, 8.8, 11.3, 14.1, 16.4 min	1	23.7 ± 4.4 m	Eibl, Hainzl et al. (2020)

Note. For geysers that exhibit changing eruption intervals merely the latest eruption interval is mentioned.

generally have distinct phases: eruption, relaxation, recharge and pre-play phase (Ardid et al., 2019; Karlstrom et al., 2013; Kedar et al., 1998; Munoz-Saez, Manga, et al., 2015; Munoz-Saez, Namiki, & Manga, 2015; Nishimura et al., 2006; Vandemeulebrouck et al., 2013; Vandemeulebrouck et al., 2014; Wu et al., 2019) (Table 1). Geysers with regular eruptive cycles are for example Old Faithful, El Jefe and Lone Star (Karlstrom et al., 2013; Kieffer, 1984; Munoz-Saez, Manga, et al., 2015). Old Faithful, US, is characterized by a two or 5 min long eruption (I) followed by a 1–3 minute long seismic coda (II) (Kieffer, 1984). Then 0–30 minutes of quiescence (III) are followed by harmonic tremor that increases gradually in intensity and amplitude (IV) before decreasing in the last 5–10 minutes (V) before an eruption (I). The total duration of the eruptive cycle follows a bimodal distribution. Munoz-Saez, Manga, et al. (2015) describe the 4 phases at El Jefe, El Tatio, Chile as eruption, relaxation (temperature and pressure drop), recharge and pre-eruptive stage with bubble addition. The eruption lasts on average 51.9 s, the quiescent Phase 80.3 s. Karlstrom et al. (2013) report the phases of eruptive cycle at Lone Star geyser, US as 28 min liquid and steam fountaining, 26 min relaxation phase without discharge from the vent, 59 min of recharge in which the geyser refills, 69 min of pre-play with series of 5–10 min long pulses of steam-water discharge.

While these geysers have a characteristic eruptive cycle, prominent differences are the duration of the cycle (Table 1) and phases, the timing when the conduit refills, and whether the geyser exhibits small eruptions shortly before the main eruption. In addition, some geysers do not show these general characteristics (Munoz-Saez, Namiki, & Manga, 2015), while other geysers sometimes skip a phase (Kieffer, 1984). Internal structures such as bubble traps and driving mechanisms might be responsible for regular or irregular eruptions and eruptive cycles.

Partly motivated by incomplete understanding and high level of complexity, experiments at geysers became larger and more multidisciplinary in recent years including instruments such as seismometers, tiltmeters, gravimeters, GPS, lidar, pressure, temperature, acoustic and geochemical sensors, infrared and video cameras and discharge measurements (Dawson et al., 2012; Munoz-Saez, Manga, et al., 2015; Nishimura et al., 2006; Namiki et al., 2014; Vandemeulebrouck et al., 2014; Wu et al., 2017). These multidisciplinary recordings were combined to study the eruptive cycle (Karlstrom et al., 2013; Kedar et al., 1996; Kieffer, 1984;

Nishimura et al., 2006; Vandemeulebrouck et al., 2014), the underlying mechanisms driving eruptions (Kedar et al., 1998; Vandemeulebrouck et al., 2014) or the structure, geometry and location of the geyser, its conduit and bubble trap(s) (Ardid et al., 2019; Belousov et al., 2013; Cros et al., 2011; Kieffer, 1984; Munoz-Saez, Manga, et al., 2015; Munoz-Saez, Namiki, & Manga, 2015; Namiki et al., 2014; Nishimura et al., 2006; Rudolph et al., 2012; Vandemeulebrouck et al., 2013; Vandemeulebrouck et al., 2014; Walter et al., 2020; Wu et al., 2017; Wu et al., 2019) (Table 1).

Eruptions and the time period up to 25 s after the eruption of Strokkur geyser, Iceland, were first studied in 1967 with one single seismic station (Rinehart, 1968). While seismic signals were discussed and generating processes suggested (Kieffer, 1984; Rinehart, 1968), the details of the eruptive cycle and underlying water reservoir system remained elusive. The uppermost part of the conduit has a complex and possibly fracture-controlled conduit geometry as inferred from submerged underwater cameras (Walter et al., 2020). Further hints on a possibly common bubble trap were extracted from the eruption interval statistics of a catalog with 73,466 eruptions containing single to sextuple eruptions (Eibl, Hainzl, et al., 2020).

To link the surficial observations to processes at depth, here we use a multidisciplinary network of seismometers, one tiltmeter, video cameras and pressure sensors (Section 3) and the yearly seismic dataset and eruption catalog (Eibl et al., 2019; Eibl, Walter, et al., 2020). We describe the eruptive cycle (Sections 4.1 and 4.3) and seismic source locations (Section 4.2) of Strokkur in June 2018. We discuss the eruption (Section 5.1), the post-eruptive conduit refilling (Section 5.2), the recharge including gas refilling of the chamber (Section 5.3) and bubble collapses at depth in the conduit (Section 5.4) in unprecedented detail. We discuss the 4 phases of the eruptive cycle (Section 5.5), the mechanism leading to multi-tuple eruptions (Section 5.6) and the location of the feeding chamber with respect to the conduit (Sections 5.7 and 5.8).

2. Field Site of Strokkur Geyser

Strokkur is located in the geothermal valley Haukadalur in southwest Iceland (Figures 1a–1c). It is a 3 km^2 area of intense thermal spring and geyser activity (Bunsen, 1847; Descloizeaux, 1847) that has been mapped and monitored in the field (Torfason, 1985, 1995) hosting nowadays over 360 hot spots as identified in thermal drone data (Walter et al., 2020).

Nowadays, Strokkur is an episodically erupting geyser with a water filled pool of 12 m diameter on the surface (Rinehart, 1968) which hosts a central about 2.2 m wide conduit (Walter et al., 2020). The system is artesian with constant outflow of water from the pool. Note that water can be in the pool while the upper part of the conduit is empty due to a sinter ring around the conduit. While the central conduit is circular on the surface, it narrows down to ∼1.2 m at 5 m depth and is elliptical at ∼9 m depth with an N-S to NE-SW trend inferred to be structurally controlled. At 12 m it widens again and becomes elliptical again at ∼16–18 m depth. At a depth of ∼22 m submerged cameras showed a drillhole that released bubbles into the conduit (Walter et al., 2020). This hole was drilled 39.4 m deep in 1963 to reactivate the geyser activity since it became dormant after an earthquake in 1896 (Torfason, 1985, 1995).

Torfason (1995) described a mean eruption frequency in 1994 of 7 min and an inflow to the geyser of 2 l/s. Newer studies report that Strokkur erupts in eruptions with one to six distinguishable water fountains (Eibl, Hainzl, et al., 2020). Water fountains within a multi-tuple eruption are spaced on average 16.1 s apart. Mean waiting time after single to sextuple eruptions increases linearly from 3.7 to 16.4 min, respectively, while the amplitude or type of the next eruption cannot be predicted (Eibl, Hainzl, et al., 2020).

3. Experimental Setup 2018 and Method

We monitored the eruptions of Strokkur from June 6–10, 2018 using two video cameras, two pressure sensors, five seismic stations installed at seven different locations (7L seismic network) and one tilt sensor (Eibl, Mueller, et al., 2020). Due to tourist activities during daytime and available working agreement, we only recorded during night-time, and de- and re-installed nearby instruments daily. The statistical analysis of eruption intervals over a period of 1 year in 2017/2018 (Eibl, Hainzl, et al., 2020) confirmed that eruptions at Strokkur are repeatable. Therefore, recordings from instruments recording at different times can be compared for different eruption types.
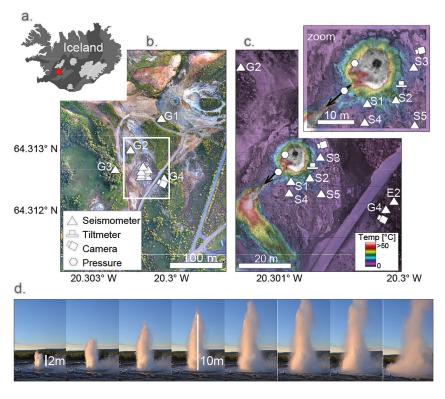
Figure 1. Overview of instrument network around Strokkur geyser. (a) Inset of Iceland with geyser location marked (red triangle), (b) Aerial map generated from camera drone. Symbols indicate instrumentation type and location. (c) Aerial map. Color shading represents thermal infrared pattern (Walter et al., 2020), highlighting the pool and its outflow channel (black arrow). Note location of seismometers (white triangles), cameras (camera symbol), tiltmeter (plate symbol) and pressure-temperature sensors (hexagon symbol), enlarged in upper right insert. (d) The height of the eruption sequence is estimated from video records.

3.1. Video Cameras, Pressure Sensors, and Tiltmeter

Video JVC cameras type GC-PX10 were placed 5 m from the pool and at 40 m distance southeast of the pool to record the bubble growth and water fountain, respectively. Cameras were installed to record video files at 1920 × 1080 pixels with a temporal resolution of 50 frames per seconds (fps). We used a Sobel edge detection algorithm (Zhang et al., 2009) on the camera data to estimate the height of some eruption fountains (Figure 1d). The camera was time synchronized by holding a GPS-clock in front of the lens at the beginning and end of each video.

To measure pressure and temperature we placed a diver (Keller DCX 22) inside the pool and one in the outflow channel (Figure 1) both covered by a few centimeters of water. In total we recorded 11.5 h of pressure and temperature data at a sampling rate of 1 Hz. These measurements indicate water level changes in the pool (not the conduit) associated with different phases of Strokkur.

We placed the biaxial platform tiltmeter (Jewell Instr. 701-2 (4X)) close to the pool (Figure 1c). It was oriented with its *x* axis pointing toward the center of the conduit on the surface and the *y* axis pointing tangential to it. Data were collected every 0.5 s by the tiltmeter and oversampled by and stored at a rate of 50 Hz at the data cube, with time synchronization by in-built GPS. We lowpass filter the tilt data with a corner at 1 Hz to avoid aliasing effects before downsampling to 8 Hz.

3.2. Seismometers

Three Nanometrics Trillium Compact Posthole 20 s broadband seismometers (installed at locations S2, S3, S5, G4) and two Nanometrics Trillium Compact 120 s (installed at locations S1, S4, E2) were linked to data cubes for data collection. G1 to G4 recorded data at 200 Hz sampling rate from June 27, 2017 to June 6, 2018

(Eibl, Hainzl, et al., 2020; Eibl, Walter, et al., 2020) and were used for eruption cycle statistics. Their recording is not good enough for a tremor location. Stations S1–S5 were installed on June 10, 2018 (sampling rate 400 Hz) for 4.5–5.25 h at 5–14 m distance south and east of the pool on the sinter surface (Figure 1) and allowed tremor locations.

The seismic data were detrended, tapered, instrument corrected and filtered. We studied the seismic data with respect to frequency content, amplitude, timing between consecutive eruptions and source location using Python toolboxes (Heimann et al., 2017; Megies et al., 2011).

The covariance matrix of the E, N, and Z ground motion was calculated in 1 s long time windows at stations S1–S5 (Figure 1). We calculate eigenvectors and eigenvalues (Bopp, 1992) to approximate the shape of the particle motion ellipse in 3D. The two largest Eigenvalues were used to calculate the linearity of the ellipse: $Lin = 1 - \sqrt{l_2 / l_1}$ where eigenvalues $l_1 > l_2 > l_3$. We calculated the azimuth measured clockwise from North and apparent incidence angle (Bopp, 1992) assuming a radial polarized ground motion according to: $Az = arctan\ (e_E, e_N)$ and $Inc = arctan\left(\sqrt{e_E^2 + e_N^2}, e_z\right)$ where Az and Inc are corrected if $Inc > 90°$ to: $Az' = Az - 180°$ and $Inc' = 180° - Inc$.

In each 1-s-long time window, we calculate all intersection points of the beams for the five seismometers S1–S5. We only allowed intersection points in the range of 64.3122–64.3136 N and 20.3023–20.2997 W. Of all intersection points within that window we calculated the mean and standard deviation. This mean latitude and longitude is defined as the source epicenter. We estimate the uncertainty of the epicenter from the statistics of the intersection points and filter for points with an uncertainty of less than 90% of the mean standard deviation that is, uncertainties of less than 9.4 m in latitude and 11.9 m in longitude.

The source depth was estimated for each station separately from the vertical projection of the epicenter to the linear strokes defined by the incidence angles at each station (Figure S4). We further derive a median depth and standard deviation in each time window from the depths at stations S1 to S4. Station S5 was discarded due to low linearity, indicating no linear particle motion and hence a less reliable depth estimate (Figure S1).

We varied the window length from 0.025 to 2 s and the frequency band in the range 1–27 Hz while testing narrow and wide frequency bands. Shorter windows and higher frequencies increased the scatter of the source location in time, but did not lead to more consistent incidence angles. We obtained the best locations in the range from 3 to 9 Hz using a 1 s long time window.

4. Results

4.1. Eruptive Cycle for Single Eruptions

Based on observations from video camera, pressure, tilt and seismic data (Figure 2), we characterize a typical eruptive cycle of a single eruption. Duration and amplitude of these observables vary slightly for different eruptive cycles (Figure 3b). The convention is to use the onset of an eruption as start of an eruptive cycle (Kieffer, 1984). Based on the characteristics of an eruptive cycle we subdivide it into the 4 phases that will be detailed in the following: (i) Eruption, (ii) conduit refilling, (iii) eruption coda and (iv) regular peaks in seismic, tilt and pressure data.

4.1.1. Phase 1: Conduit Eruption

An eruptive cycle of Strokkur starts with a rising gas bubble that deforms the water surface above the conduit into an about 2 m wide and 40 cm high blue bulge. The bulge becomes white when the rising gas bubble reaches the surface. The bubble surface ruptures, the steam and water mixture jets into the air into a high fountain (Figure 2a).

At the same time the seismic amplitude increases above the noise level 2–3 s before it peaks and decreases (Figure 2). During most eruptions the seismic amplitude is increased for less than 5 s and has at 40 m distance energy between 1.2 and 160 Hz (Figures S2b–S2f) with most energy around 20 Hz (Figure 2d). The eruption is accompanied by a drop in linearity, azimuths pointing toward the conduit and incidence angles around 90° (Figure S1). On June 7, 2018 at 5:20:00 both the elevated seismic amplitude and bulge formation
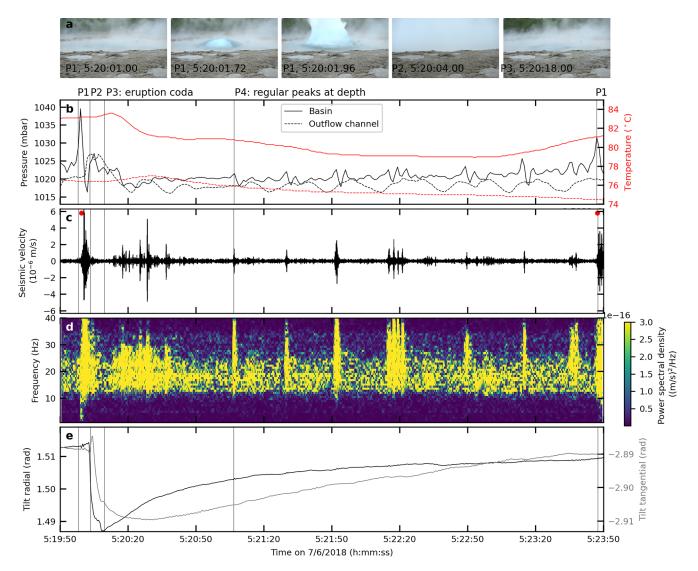
Figure 2. The eruptive cycle of Strokkur on June 7, 2018 from 5:19:50 is subdivided into four phases. (a) Photos from Phase 1 (P1), 2 (P2) and 3 (P3). Photos in Phase 4 (P4) are similar to Phase 3. (b) Pressure (black) and temperature (red) measured by the pressure sensor in the pool (solid) and outlet (dashed). Phase 1 to Phase 4 marked as P1 to P4, respectively. Gray vertical lines marks start of phases. (c) Vertical seismic ground motion at station E2 filtered 1–40 Hz. Red dots mark eruptions as in (Eibl et al., 2019). (d) Spectrogram of subfigure c with 2.56 s window length and 2.28 s overlap. (e) Radial and tangential tilt recorded about 3 m from the pool.

and eruption persisted for 2 s. The highest seismic amplitude and broad frequency content correlate with the time of the water fountain and water splashing on the ground.

At 4 m distance east of the pool the radial and transverse tilt signal exponentially increased (Figure 2e).

Similarly, the pressure sensor in the pool recorded an exponential increase shortly before an eruption. The eruptions caused a pressure increase of 8–32 mbar on June 7, 2018 (Figure 3) which corresponds to a water wave of 8–32 cm height. The pressure sensor in the outlet recorded a broader pressure increase of 3.5–10 mbar shortly after eruptions and fluctuations of ± 2 mbar between eruptions. Within the whole week the measured temperature peaked at 82–87°C about 15 s after the pressure peak.

4.1.2. Phase 2: Refilling of the Conduit

The water fountain and pool overflow cause a water loss from the pool and conduit while water splashes on the ground (Figure 1). Due to a sinter ring around the conduit, the water level in the pool lowered a few centimeters (pressure drop of about 2–3 mbar, Figures 3a and 2a) while the water level dropped more than
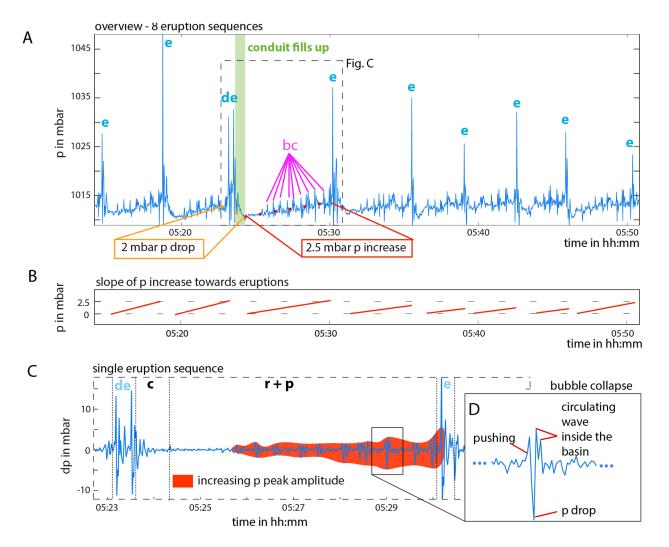
Figure 3. Typical pressure sensor recording inside the geyser pool. (a) Sequence of eight eruptions where eruptions (e), double eruptions (de), peaks in pressure (bc) are marked. The pressure data revealed a certain range of pressure conditions in the pool, that are affected by the eruptive behavior, like pressure drop during and increase after eruptions. (b) Pressure increase at the sensor caused by water level changes vary slightly in amplitude and frequency from cycle to cycle. (c) First deviative of pressure shown in subfigure a for a single eruption sequence. The intensity of bubble collapses toward an eruption seems to increase. (d) shows a typical sequence of a bubble collapse, starting with a slight positive peak, followed by a larger pressure drop and following positive peaks, that are likely caused by traveling waves inside the pool.

1 m inside the conduit. However, the conduit refilled within 15–20 s (green bar in Figure 3a) with water from depth, from a shallow aquifer and from the surface flowing back into the pool as seen in video camera data inside the conduit (Walter et al., 2020). This filling is accompanied by a large amount of small bubbles on the surface. In this time period the seismic amplitude is low for about 8 s, the amplitude on the radial and transverse tilt component decreased and the pressure sensor records a calming down in the pool (Figures 2b, 2c, and 2e).

4.1.3. Phase 3: Eruption Coda

Consequently, the tilt signal logarithmically converged toward the original level shortly before the next eruption (Figure 2e). The first part of this period is characterized by a water filled conduit whose surface is ruptured by a large amount of about 1 cm large bubbles, constant pressure in the pool and the seismic "eruption coda" (Figure 3). The eruption coda occurs on average 13.10 ± 3.97 s after the beginning of the last water fountain of an eruption (Kieffer, 1984; Eibl, Hainzl, et al., 2020). It is dominated by on average 19 ± 4 repeated, regular bursts at a mean spacing of 1.52 ± 0.29 s (Table S1). The temporal spacing increases from 1.5 to 1.6 s in time (Figure 5g). These bursts have energy between 3 and 71 Hz at 40 m distance

southeast of Strokkur with most energy between 10 and 30 Hz (Figure S2c–S2e). The amplitude envelope of all events in this phase is asymmetric that is, the peak amplitude increases fast, then decreases slowly (Figure 5h) and is visible above the noise level for on average 26.1 ± 6.9 s (Table S1). Azimuths point to a location at depth west of Strokkur with a higher linearity.

4.1.4. Phase 4: Regular Peaks in Seismic, Tilt, and Pressure Data

While the tilt keeps increasing, the second part of this period is characterized by a calm water surface ruptured by a few cm large bubbles, a slowly rising pressure and water level (cm range) in the pool (Figure 3a) intersected by regular peaks in seismic amplitude accompanied by small water level drops in the conduit.

The seismometer recorded on average 8 ± 2, 0.5 s long amplitude peaks (Figures S2c–S2e) in a 2.3 ± 0.7 min long time interval (Table S1) at a spacing decreasing from 25 to 22 s (Figures 5a and 5i). Similarly, the amplitude of the bursts decreases with time toward the next eruption (Figure 5a). The first seismic amplitude peak occurs on average 0.94 ± 0.19 min after the beginning of a single eruption (Figure S3). These peaks are shorter in duration than during eruption and have a frequency content of 3–160 Hz (Figure S2). In some cases, a short and weak eruption coda is visible.

Times of seismic peaks (located in the conduit at depth) are accompanied by a 1 s long drop of the water column by a few centimeters inside the conduit. Since it generates small waves in the pool reflecting off edges the pressure sensor detects ∼3 mbar pressure peaks (Figures 2 and 3c).

Pressure peaks usually start with a slight positive pulse, followed by a larger negative peak (Figures 3a and 3d). The first derivative of the pressure signal (Figure 3c) reveals an increasing amplitude of the pressure peaks toward an eruption. However, the last peak before the eruption tends to be smaller while the waiting time after the last visible pressure peak is in a small range of 10–20 s.

4.2. Seismic Source Location

Throughout the eruptive cycle most of the seismic signal has a frequency content with most energy between 10 and 30 Hz. During seismic amplitude peaks in Phase 1 and 4, the frequency content is higher with energy up to 71 Hz. Due to stronger attenuation of higher frequencies this may indicate a smaller distance to the seismometer.

In the 3–9 Hz frequency band, the tremor locations cluster in two dominant source locations. A deeper tremor source persists in Phase 2 and 3 and most of the time in Phase 4. This tremor source is characterized by a high linearity and hence a reliable depth estimate. Mean depths are 23.7 ± 4.4 m, while it is located 13–23 m west of the location of the conduit on the surface (Figure 4). The tremor is most focused in this region during the eruption coda.

The second tremor source peaks at 9.9 ± 4.1 m (Figure 4d). These peaks have low linearity on all stations and hence less reliable depth estimates (Figure S1). Its latitude and longitude coincide with the location of Strokkurs' conduit on the surface. The shallow depths correlate with times when either eruptions (Phase 1) or peaks in Phase 4 occur. During peaks in Phase 4, the tremor source is located as shallow as about 5 m (see Discussion on Limitations).

4.3. Eruptive Cycle for Double to Sextuple Eruptions

Each eruptive cycle contains all four phases independent of the eruption type (single to sextuple eruption) where Phase 1, 3, and 4 persist longer for eruptions with higher multiplicity.

The eruption and Phase 1 persist as long as water fountains occur at an average spacing of 16.1 ± 4.8 s (Eibl, Hainzl, et al., 2020). The duration of Phase 1 linearly increases from single to sextuple eruptions with 1–6 water fountains, respectively. We note that Phase 2–4 only follow the last water fountain in a multi-tuple eruption while the first ones are merely followed by another water fountain.

The period from the beginning of the last water fountain within an eruption sequence to the beginning of the coda is constant across all event types and in the range of 12.8–14.5 s (Figure 5 and Table S1). This period includes the last water fountain in Phase 1 and the low seismic amplitude (Phase 2). In double eruptions,
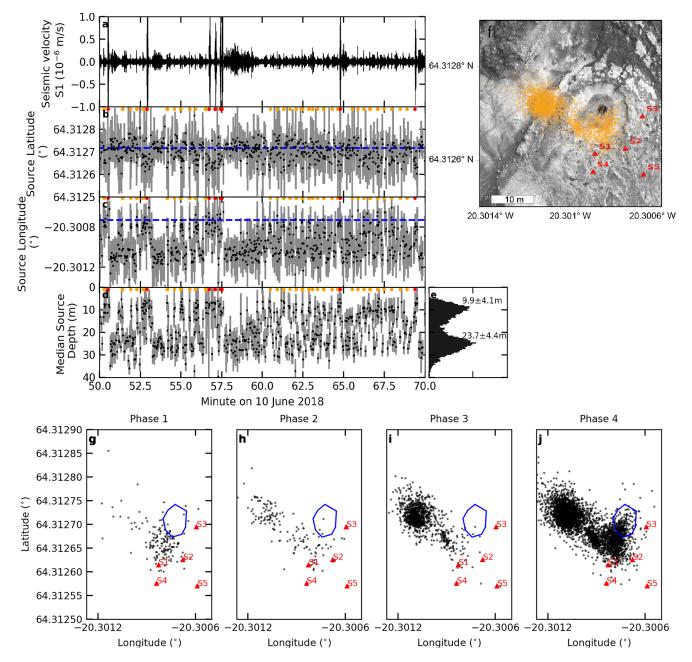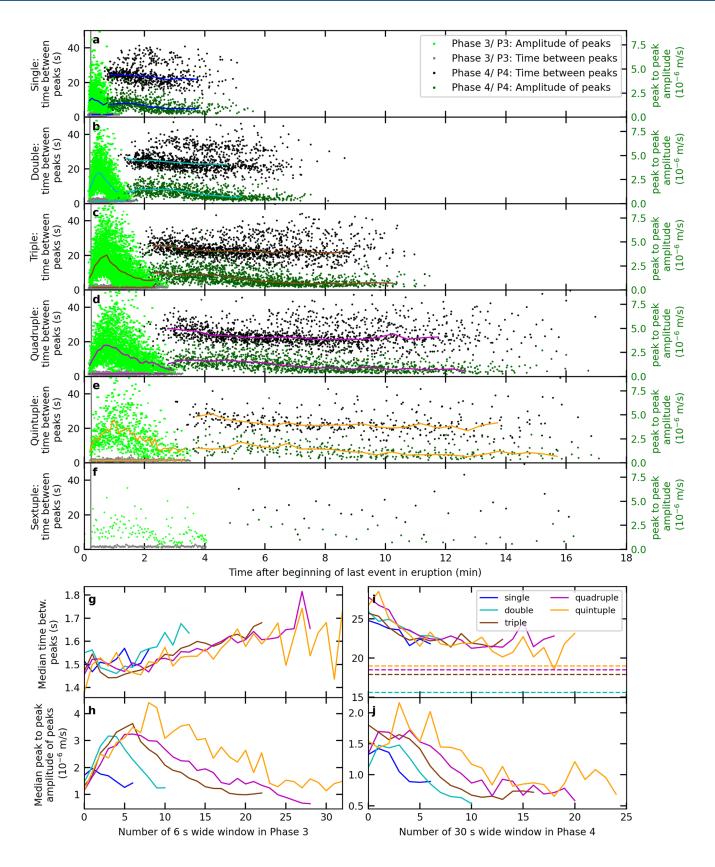
Figure 4. Seismic tremor location on June 10, 2018 in 1 s long time windows filtered 3–9 Hz. (a) Seismic velocity seismogram of station S1, (b) Mean latitude and (c) mean longitude for intersection points of beams projected from stations S1 to S5 based on the respective back azimuth. Peaks in Phase 4 (orange dots), eruptions (red dots) and location of Strokkur (blue dashed line) are marked. (d) Median depth and one standard deviation of four depths derived from mean latitude, mean longitude and incidence angles at stations S1–S4. (e). Histogram of subfigure (d) with dominant depth ± one standard deviation. (f–j) Projection of the best constrained points from subfigure b and c where the standard deviation of the latitude and longitude intersection points was less than 9.4 and 11.9 m, respectively. (f) all and (g–j) sorted according to phases.

the first drop in tilt is immediately followed by an exponential increase and a second drop leading to a total larger drop.

The seismic eruption coda in Phase 3 linearly increases in duration from 26.1 ± 6.9 s to 230.7 s while the number of peaks increases from 19 ± 4 to 142 for single to sextuple eruptions, respectively. The mean spacing between the seismic peaks is similar across eruption types and in the range of 1.52–1.64 s (Table S1). The peak seismic amplitudes in the eruption coda are slightly larger for eruptions with increasing multiplicity but follow a similar fast increasing, then slowly decreasing amplitude trend (Figure 5h).

The mean waiting time from the beginning of the last water fountain in an eruption to the first seismic or pressure peak in Phase 4 linearly increases from 0.94 ± 0.19 min for single eruptions to 4.83 min for the sextuple eruption (Figure S3 and Table S1). Phase 4 persists for 2.3 ± 0.7 to 11.4 min (linearly increasing) with 8 ± 2 to 29 peaks at a mean spacing in the range of 23.3 ± 7.2 s to 25.4 ± 6.3 s. The peak spacing at the start of Phase 4 increases from 24 to 28 s for single to quintuple eruption, respectively, while the spacing at the end of the cycle is comparable across eruption types ($\sim$21 s). For all eruption types both the peak spacing and seismic amplitude in Phase 4 decrease with time (Figures 5i and 5j).

5. Interpretation and Discussion

We developed a conceptional structural model of the shallow plumbing system of Strokkur geyser (Figure 6). It consists of a 35 m long vertical channel with variable cross-section feeding the central surface pool at Strokkur. Hot water continuously drains from the pool through a small trickle. The depth and geometry of the conduit were derived from video camera measurements (Walter et al., 2020). The depth was measured based on the length of the string that was used to move the camera downwards. Depths in the conduit might be overestimated. Based on our tremor locations, our model has at least one sealed bubble reservoir (bubble trap) located at a mean depth of 23.7 ± 4.4 m and 13–23 m west of the central pool and its feeder channel.

In accordance with findings at geysers worldwide (Table 1) we subdivide the eruptive cycle of Strokkur into four phases (Figure 6). These comprise the conduit eruption (Phase 1), the refilling of the conduit (Phase 2), the gas filling of a bubble trap (Phase 3), and bubble flow into the conduit and collapse at depth (Phase 4).

We first discuss processes and signals observed during the individual phases, and then compare the structural process model of Strokkur to other geyser models. We finally discuss possible mechanisms leading to single and multi-tuple eruptions.

5.1. Phase 1: Conduit Eruption

The eruptive phase at Strokkur starts when the rising bubble slug approaches the surface and pushes the water column out of the conduit. A blue water bulge forms immediately before the steam jet eruption. Minutes before the bubble bursts, signals such as the decreasing audible and tangible ground motion, the decreasing seismic peak amplitude, the logarithmic converging tilt motion and increasing pressure peaks measured in the pool, were detected. We classify them as long-term eruption precursors. Short-term eruption precursors at Strokkur are in the order of seconds and comprise the increasing seismic amplitude and exponentially increasing tilt signal. We interpret these short-term precursors as caused by the rising slug after it reached the shallowest part of the conduit. It deforms the edifice and is recorded as an increasing seismic noise while it moves toward the surface.

We detect the increasing seismic noise at Strokkur only about 2–3 s before it peaks because the source is too far or too weak to be detected beforehand. This amplitude increase might however also be linked to the widening of the conduit that was inferred from video camera data at a depth of 7 m. James et al. (2006) reported in a laboratory study on a gas slug that acoustic and inertial resonant oscillations can be stimulated by a pressure difference (increase above, decrease below) induced by a gas slug undergoing a change in flow pattern when migrating into a wider conduit.

The decompression of the fluids in the bubble trap has two effects: (i) it causes the steam to adiabatically expand, and (ii) it causes some fraction of the liquid volume to flash to steam. Both of these effects increase the volume of the trap fluids, which expels fluid from the system and sustains an eruption (Grant

Figure 5. Temporal spacing and amplitude of seismic peaks in Phase 3 and 4 for each eruption type. (a–f) Spacing between peaks in Phase 3 (gray) and 4 (black), amplitude of peaks in Phase 3 (light green) and 4 (green) for (a) 129 single eruptions including the 17 largest, (b) 144 double, (c) 109 triple, (d) 80 quadruple, (e) all 17 quintuple and (f) all 1 sextuple eruptions. Vertical gray line marks onset of Phase 3. Colored lines are medians of each dataset compared across eruption types in subfigure g–j. (g–j) Median spacing and amplitude in time Phase 3 and 4 for all eruption types. (g) The median temporal spacing and (h) amplitude of peaks in Phase 3. (i) Median temporal spacing and (j) amplitude of peaks in Phase 4. Horizontal dashed lines in (i) mark the spacing between multiple water fountains within a multi-tuple eruption (Eibl, Hainzl, et al., 2020).
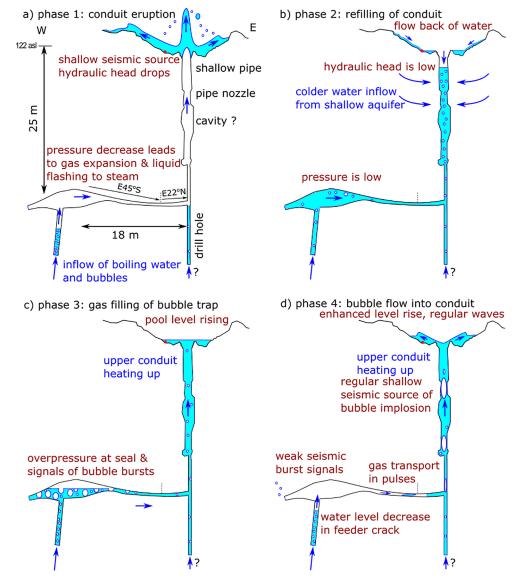
Figure 6. Schematic diagram illustrating conduit and plumbing system of Strokkur geyser and the processes occurring during phases 1–4. The location, geometry and width of the conduit and the sealed bubble reservoir (bubble trap) are based on direct video camera data (Walter et al., 2020) and tremor locations in this study. The eruptive cycle at Strokkur is divided in four phases: (a, Phase 1) the eruption (b, Phase 2) the immediate flow back of water and refilling of the upper conduit, (c, Phase 3) the gas refilling of the bubble trap reservoir at depth and (d, Phase 4) the migration of bubbles from the bubble trap into the conduit and their collapse at depth in the conduit. The observations from different sensors (pressure sensor = red dot) and the hydromechanical processes occurring during each phase are denoted by reddish text.

& Sorey, 1979). While water jets into the air, water waves travel from the conduit to the sides of the pool. These waves and the reflected water waves in the pool are detected by the pressure sensor. While water splashes on the ground and generates a chaotic seismic wavefield of white noise for a time period of about 5 s, seismic amplitudes slowly decrease. It is therefore difficult to determine the length of the eruption from the seismic signal. If we discard the shape of the seismic signal caused by an individual water fountain and assess the duration of the total sequence of water fountains, Eibl, Hainzl, et al. (2020) found a correlation between eruption duration that is, number of water fountains and waiting time after an eruption. A similar correlation was found at other geysers (Azzalini & Bowman, 1990; Gouveia & Friedmann, 2006; Namiki et al., 2014; Rinehart, 1965).

The tilt and seismic noise short-term precursors are also found at other geysers. However, Kedar et al. (1996); Kedar et al. (1998) interpret a seismic signal at Old Faithful that gradually emerged from the white noise (10 Hz to above 40 Hz) as having "no clear precursor." The water falling at Old Faithful lasts 1–3 min (Kedar et al., 1998). Nishimura et al. (2006) recorded a slower, linear increase and uplift on the radial tilt component which started shortly before the eruption of Onikobe geyser reached its end and can therefore be used to predict when the eruption is over and whether the eruption is short or long. Munoz-Saez, Manga, et al. (2015) report that eruptions in El Tatio are accompanied by tilt on both components. Tilt increases in the recharge phase and peaks on the radial component during the eruption potentially due to water ponding in the pool. The tilt drops before the eruption is over, which might be an effect of the water pond and the curve is in general not that steep as at Strokkur. The latter might be caused by a larger distance from the vent in the El Tatio study (Munoz-Saez, Manga, et al., 2015). Tilt at Calistoga Geyser drops after the infrared intensity reached maximum intensity and the geyser erupts (Rudolph et al., 2012). Tilt increased during an eruption of El Cobreloa and decreased slowly afterward until the next eruption (Munoz-Saez, Namiki, & Manga, 2015). They argue that this reflects recharge in shallow aquifers while increasing tilt as measured near Strokkur or other geysering wells (Nishimura et al., 2006; Rudolph et al., 2012) reflects changes in deeper reservoirs. We infer from our dataset that the eruption releases bubbles from such a deep reservoir. For the depth estimate see Section 5.8.

While the system looses energy in an eruption, here we find that the pool temperature increases after an eruption. This might indicate that after an eruption the pool is filled with fluids that were much deeper in the system prior to the eruption, and thus are intrinsically hotter. The subsequent decrease in temperature is due to evaporation and cooling of the large and shallow pool via heat transfer to the atmosphere.

5.2. Phase 2: Refilling of the Conduit

In Phase 2 Strokkurs' conduit was partly emptied by the eruption, the water is still in the air and splashing back on the ground or is drifting away as steam. While surficial water flows back into the pool and conduit, colder water flows into the conduit from a shallow aquifer and the deep bubble trap is full of hot water flowing in from depth. Strokkurs' conduit refills within about 10–15 s.

The temperature in the pool is highest in this period and peaks after the eruption. Our findings contrast Nishimura et al. (2006) who reported a 64°C increase in temperature about 50 s before an eruption. The radial tilt signal strongly decreases in Phase 2 and more strongly in double eruptions. Nishimura et al. (2006) interpret such a trend as water removal in the conduit and deep chamber. The seismic amplitude in this time window is low in accordance with the observation that eruptions of Strokkur correlate with seismic signals, that stop before the conduit is refilled (Kieffer, 1984).

This silence might be due to the gravitational pressure increase in the conduit and plumbing system related to the recovery of the hydraulic head, which suppresses bubble formation at depth. This mechanism has been suggested at Old Faithful geyser (Kieffer, 1984). However, (Kieffer, 1984) report two periods of reduced seismicity of up to a minute in duration during the recharge process. Seismicity is reduced (i) when water rapidly rises in the conduit and the pressure increase suppresses steam bubble formation or (ii) shortly before eruptions when bubbles are in a zone of boiling that is acoustically decoupled from the conduit wall (Kieffer, 1984). Here, we observe only one period of reduced seismicity. Additionally, the reduction of seismic amplitude after eruption is also possible due to the deeper source excitation which induces greater attenuation from geometrical spreading. This is true and observed for Strokkur in this study, and for Old Faithful from Wu et al. (2019).

5.3. Phase 3: Gas Filling of the Bubble Trap

In Phase 3, gradually increasing tilt and linearly increasing pressure in the pool indicate that the water level in the pool gradually rises and the system starts to pressurize at depth. We observe weak and regular seismic peaks (eruption coda), which we associate with bubble bursts at the gas-water contact in the bubble trap.

After the eruption the temperature of bubble trap fluids will be at a minimum due to energy loss during the eruption and the reduced hydrostatic load which slightly decreases the saturation temperature. At the

beginning of Phase 3 steam entering the bubble trap is more likely to collapse when encountering subcooled liquids in the trap. This condensation releases latent heat to the liquid phase and increases its temperature. Toward the end of Phase 3 it becomes easier for the steam to ascend through the liquid without condensing, to mix with the overlying steam phase and to increase the gas volume in the trap. Hence, rising hot water and bubble nucleation in the bubble trap lead to a steadily growing gas volume and temperature below the sealing cap of the trap. This might push the fluids into the conduit and increase the water level in the pool as visible on the pressure sensor.

While gas accumulates and coalesces the gas-water contact migrates downwards in the bubble trap. We speculate that seismic peak amplitudes in this phase increase when the volume of accumulated gas and the temperature in the underlying water increases. The eruption coda ends when the trapped gas has displaced the underlying water into the deeper part of the feeder conduit. Both, the liquid and the vapor phase in the bubble trap are loaded by the overlying water in the conduit system (and pool). The vapor and co-existing liquid remain in thermodynamic equilibrium and are at their contact point at the same temperature and pressure. This can only be disturbed if the system fluids move rapidly for example, during an eruption (Phase 1).

Rinehart (1968) reported that the eruption coda at Strokkur consists of 4–5 impulsive, mainly upward directed 1–2 s long bursts at a spacing of 2–3 s in a time interval 9–25 s after eruption. Our findings differ since we found 18–142 peaks in the eruption coda with energy in both directions (up and down) starting 12.6–14.5 s after the beginning of the last water fountain of an eruption sequence. Assuming an eruption duration of less than 5 s, the coda starts about 7–9 s after the eruption end and persists more than 25 s. We find that bursts were spaced merely 1.53–1.64 s apart and have a duration of less than 1 s. We therefore only agree on the start time of the coda after eruption and the duration of single bursts. The discrepancy in coda duration or burst spacing might be due to a longer time series we analyzed or changing behavior of the geyser.

Rinehart (1968) further reported that within the series of bursts the first two to three were audible, while we could hear and feel none of the seismic peaks in the eruption coda. Rinehart (1968) attribute the eruption coda to the refilling of underground cavities and slashing of water in a reservoir at depth. They noted that the spacing between these peaks increased in time and interpret it as more slowly moving water splashing from side to side. Here, we confirm this increase in spacing but disagree with the interpretation of water splashing from side to side.

Besides increasing gas volumes or increasing area of the gas-water interface, an increased acoustic impedance mismatch between the water-steam mixture and the conduit walls such as suggested in Kieffer (1984) at Old Faithful, US, might dampen the bursting of these bubbles when the bubble trap is filled with bubbles. Similarly, Kedar et al. (1998) observed a water pressure peak inside the conduit of Old Faithful followed by a seismic peak and therefore link tremor to impulsive events. Tremor increased in amplitude when more impulsive events were present. However, Kedar et al. (1998) also observed that the widening of the conduit during the upwards motion led to a decrease in event number in time while the water level was rising and heat was put in. The tremor amplitude was therefore modulated by the conduit geometry. Here at Strokkur, we do not observe this.

5.4. Phase 4: Bubble Collapses in the Conduit at Depth

The experimental study of Jaupart and Vergniolle (1988) studied rising gas bubbles in a fluid of different viscosities. Bubbles accumulated at the top where the tank was closed apart from a small open conduit. They describe that gas bubbles accumulate and coalesce while part of the foam flowed into the conduit and collapsed on the top. Bubbles coalesce if the foam reaches a critical thickness (dependent on viscosity) and collapse instantly to a single large gas pocket in low viscous fluids. Bubble coalescence and eruption is only possible if foam reaches critical thickness, else there is bubbly flow. The time between two pockets is the time needed to reach the critical thickness again. We presume that Strokkur behaves similarly in Phase 4.

In Phase 4, the system keeps recharging at depth and bubbles are added to the filled bubble trap. However, first bubbles escape through a narrow crack into the conduit to form a bubble piston. The recordings of a video camera that remained inside the conduit during an eruption indicates that bubbles sometimes

collapse inside the conduit without reaching the surface (Walter et al., 2020). Bubbles collapse at depth if they rise to a cooler area within the water column where the steam condenses (Kedar et al., 1998).

Bubble collapses at depth are recorded by acoustic thumps, tangible ground motion up to a few meters distance from the conduit, seismic peaks and tremor at the seismometer, a drop of the water column in the conduit leading to a sloshing water surface and waves in the pool (Figure 3d), positive pressure peaks of direct or reflected water waves and 1 s long tilt and seismic amplitude peaks with broad frequency content. These bubble collapses at depth have a weaker eruption coda.

Throughout Phase 4, several bubbles leave the bubble trap and collapse at depth in the conduit. The average spacing of 23.3–25.4 s (Figure 3a) is independent of the eruption type. We conclude that the physical conditions are comparable across eruption types once the bubble collapses start. The temporal spacing between the collapses decreases and bubble collapses follow more quickly toward the end of Phase 4. This might be due to (i) shorter distance to the collapsing locations, (ii) an increased speed of movement (iii) or faster bubble formation in the bubble trap. A shorter distance to the collapsing location seems unlikely since we expect a bubble to collapse at shallower levels toward the end of the eruption when the conduit is hotter. Unfortunately, our seismic network does not allow us to make a statement on relative source depths of bubble collapses within a cycle. We speculate that the bubble moves faster toward the end of the cycle possibly due to an increased temperature in the conduit or a larger vertical dimension of the slug. However, they might also be formed faster in the bubble trap while the temperature increases.

Bubbles might collapse (i) at the same location or (ii) at shallower levels. Bubbles could collapse at the same depth for example, in an always colder region of the conduit. If bubbles collapsed at the same depth they would need to increase in size to cause larger waves in the pool after collapse. Alternatively, bubbles could reach shallower depths with time as the conduit heats up and allows bubbles to move further before they reach conditions for collapse. Shallower collapses might generate larger waves in the pool as detected by the pressure sensor. Namiki et al. (2014) suggest that minor eruptions at El Cobreloa, El Tatio heat the conduit and allow major eruptions during which the whole water column in the conduit boils to larger depths. Minor eruptions might correspond to bubble collapses at depth at Strokkur, while major eruptions are similar to eruptions of Strokkur. Here, bubble collapses heat the conduit and hence prepare the system for eruptions.

The seismic signal caused by bubble collapses at depth becomes increasingly weaker throughout Phase 4 until it is neither felt nor heard (Figure 5). However, they are still inferred visually from the small drop of the water column inside the conduit causing waves in the pool. Both bubble collapses at the same or shallower depth cannot explain this decrease in seismic amplitude. We therefore speculate that the signals are damped when more bubbles exist in the conduit and decouple the bubble noise from the conduit walls (Commander & Prosperetti, 1989). Similarly, in the recharge phase of Old Faithful the amplitude and seismic event rate become stronger and more frequent in time before they become stable (Kedar et al., 1998). However, minutes before the eruption the amplitude drops but event rate remains stable. Periods of reduced seismicity exist up to a minute in duration in the recharge cycle (i) when water rapidly rises in conduit, water squeezes through a narrow area, pressure increases suppresses steam bubble formation below the nozzle (ii) shortly before eruptions when the water-steam mixture is in a zone of boiling that is acoustically decoupled from the conduit wall at the final, steam-rich stages of the eruptive cycle (Kieffer, 1984). At Old Faithful they interpret the drop in seismic amplitude before eruption as more microsteam bubbles which cause an acoustic impedance drop and lead to an inefficient conduction of noise.

The slightly longer duration of the single bubble events at Strokkur (0.5 s) compared to single bubble events at Old Faithful (∼0.2 s (Kedar et al., 1998)) is likely related to differences in the conduit length, shape and complexity. Larger gas bubbles may explain longer durations, however, they may also produce a larger buoyancy which can influence the dynamics and energy of the eruptions.

The seismic amplitude decrease in Phase 4 of Strokkur contrasts the slowly logarithmic converging radial tilt and pressure signal toward an eruption. The tilt indicates a pressure increase at the cap of the gas reservoir at depth. During this phase, the water level in the pool is linearly increasing, as evidenced by the pressure data measured in the pool. This indicates that water is pushed out the conduit because of the

accumulation of bubbles at depth in the bubble trap. Additionally, thermal heating and expansion of the water in the conduit may enhance the water level rise in the pool.

5.5. Eruptive Cycles at Geysers

The eruptive cycle is at most geysers subdivided into the 4 phases eruption, relaxation, recharge and pre-play with slowly filling conduits (Karlstrom et al., 2013; Kieffer, 1984). In contrast, pool geyser Strokkur lacks a pre-play phase with small eruptions and merely has bubble collapses at depth in Phase 4. This might be closer to a regular geyser in El Tatio where Munoz-Saez, Manga, et al. (2015) described an eruption, relaxation, recharge of water and bubble adding pre-eruptive stage and is identical to the bubbles migrating through a horizontal crack into the vertical conduit where they collapse and heat the conduit (Belousov et al., 2013). Hence, Phase 4 of the pool geyser reported here might correspond to the pre-play phase of cone geysers. The system is approaching thermodynamic conditions for an eruption, but has not met them yet. Small bubbles escape but do not unload the system enough to trigger an eruption, either because the bubbles are too small or the fluids in the system are not hot enough yet.

Cycles are mostly (Karlstrom et al., 2013) longer than at Strokkur but sometimes also shorter (Munoz-Saez, Manga, et al., 2015). Geyser such as Old Faithful, US, have a bimodal eruption interval, erupting on average about every 65 or 93 minutes (Wu et al., 2017). The bimodal distribution is associated with eruptive cycles without seismic quiescence. This contrasts the behavior of Strokkur where each eruptive cycle contains all 4 phases and the seismic quiescence is the only phase with constant duration across eruption types.

5.6. What Causes Multi-Tuple Eruptions?

Strokkur is characterized by single to sextuple eruptions. Multi-tuple eruptions are composed of multiple water fountains at an average spacing of 16.1 s, a larger waiting time after eruptions (Eibl, Hainzl, et al., 2020), a longer eruption coda, larger amplitude in eruption coda peaks, more bubble collapses at depth and a larger drop in tilt. We propose that more heat, gases and water are lost from the bubble trap during multi-tuple eruptions. This might happen in a bubble trap with rough surface that is fully filled when eruptions are triggered. Since we assume a constant inflow of heat at depth, it takes longer for the system to heat up and pressurize after an eruption with high multiplicity. In a multi-tuple eruption (i) bubbles of similar size might leave the bubble trap in a trail of bubbles and reach the surface if certain conditions are met or (ii) one large bubble leaves the bubble trap and is split into multiple bubbles on the way.

Eibl, Hainzl, et al. (2020) reported a mean spacing of water fountains of 15.6 ± 4.5 s to 19.0 ± 5.2 s for single to quintuple eruptions, respectively, with no clear correlation between spacing and eruption type. These values are similar to the spacing between bubble collapses at depth at the end of an eruptive cycle shortly before eruption (Figure 5i). This might indicate that in multi-tuple eruptions same size bubbles regularly leave the bubble trap and make it to the surface multiple times in a row. Inevitably, shallower and shallower collapse locations throughout the cycle would lead to an eruption. However, if bubbles collapsed at the same depth in an area of lower temperature, a closer temporal spacing of bubble collapses might heat this region up shortly and allow bubbles to pass and to reach the surface. In multi-tuple eruptions the spacing of bubbles might have decreased sufficiently to pass this location multiple times before the heat is lost again.

In multi-tuple eruptions a larger part of the bubble trap is emptied, which might lead to a larger bubble migrating into the conduit. To observe multiple water fountains on the surface this large bubble would need to be split into multiple smaller bubbles at a constriction. Contrasting the decreasing temporal bubble collapse spacing in Phase 4, Eibl, Hainzl, et al. (2020) reported an increasing spacing between water fountains with time within a multi-tuple eruption. This might support the hypothesis that a larger bubble leaves the bubble trap in a multi-tuple eruption. When it is split into multiple smaller bubbles, later ones might be smaller and travel slower.

5.7. Quality and Limitations of the Tremor Location

An uncertainty of our seismic tremor location using three components of a seismometer might be the alignment of the seismometer to geographic north, as compasses are affected by magnetic minerals in volcanic

environments. Since S1–S5 were installed near the geyser on a sinter basement it does not contain a lot of magnetic minerals that affect it. In addition, the azimuths derived during an eruption point toward the location of the conduit on the surface. We are therefore confident that our sensors are not misaligned with respect to geographic north.

We assume a linear wave propagation in a homogeneous medium to locate the source of the seismic tremor. However, we did not convert the apparent incidence angle to real incidence angle. For this correction, a plane wave front is assumed which is most likely not the case at less than 30 m distance from the source. This will lead to a possible overestimation of the tremor source depth.

Based on our waveform analysis we are confident that the seismic source mainly emits P waves. These are characterized by a linear particle motion which we use to point to the source location. Assuming a particle motion parallel to the propagation direction, the back azimuths derived for all five stations intersect laterally. We checked for S wave content assuming a particle motion perpendicular to the propagation direction and found that back azimuths no longer intersect. We are at less than 10 m distance from the geyser conduit and further assume that the P wave emitting source at depth does at this distance not create an significant amount of Rayleigh waves. Based on our analysis of the particle motions we are comfortable that we are able to make these assumptions. However, during eruptions the tremor source at Strokkur is dominated by Rayleigh waves. We note that although the eruptions occur on the surface, the source location is not at 0 m depth. This might be because a region down to a few meters is excited. However, since the linearity of the particle motion drops during eruption and Rayleigh waves dominate the waveform, the source depth might also be affected.

While most energy is located in the 10–20 Hz frequency band, we use frequencies between 3 and 9 Hz for the source locations. We are able to resolve two clear tremor locations (Figure 4). We believe that this is not resolvable at frequencies of less than 3 Hz due to a lack of energy and at frequencies above 10 Hz due to increased attenuation and scattering of the waves. In contrast to the work of Wu et al. (2019) and Vandemeulebrouck et al. (2013); Vandemeulebrouck et al. (2014) at Old Faithful we cannot resolve a robust and constrained depth for the seismic sources when filtering above 10 Hz. Our location approach yielded 5 depths estimates from five stations (Figure S4). Since installation conditions were identical these differences indicate a path effect where waves might be affected by fractures in the subsurface and the conduit or heterogeneities in the subsurface.

5.8. Depth and Location of the Bubble Trap

Throughout the cycle there are two different seismic sources present: a (i) stationary, collapsing source in the bubble trap at depth with a dominant frequency content between 10 and 30 Hz and (ii) shallow, collapsing seismic source with most energy between 3 and 70 Hz. Based on spread of the best constrained tremor locations we assume that the bubbles migrate from a wide bubble trap through a narrow SE-NW oriented crack into a SW-NE oriented fracture into the borehole where they either collapse at depth or burst on the surface (Figure 6). Video recordings did not show an eccentric conduit until about 18 m depth. As the trap is located at 23.7 ± 4.4 m depth, and 13–23 m offset to the conduit, the lateral connection might be horizontal or subhorizontal. The exact geometry is unknown. The SW-NE oriented fractures are consistent with the dominant fracture pattern in the area (Walter et al., 2020). Similar bubble trap geometries linked via narrow, horizontal cracks to a wider, highly contorted, vertical conduit were mapped in Geyser valley, Kamchatka using video cameras (Belousov et al., 2013).

Based on our locations the cause of the eruptions is not likely to be sudden boiling in the water column that forces hot water upwards. We speculate that the system consists of one large bubble trap that empties partly in single eruptions, and more thoroughly in sextuple eruptions. There are most probably no separate multiple bubble traps, unless it is one large connected bubble trap. Further research is needed to resolve the amount of emptying of the bubble trap for different eruption types and details of the bubble trap geometry.

We assume that when the bubbles collapse they squeezed through the borehole from the drilling in 1963 since depth locations indicate a depth around 9.9 m and since video camera observations (Walter et al., 2020) show bubble collapses at less than 18 m depth. This location is beneath stations S1 and S2 that show the most pronounced drop in linearity and change in azimuth (Figure S1). At Old Faithful Cros et al. (2011)

used a Matched Field Processing technique to locate a 10 min long window of regular seismic peaks about 20 min before an eruption at 12 m depth in the conduit. They interpret them as bubble collapses in the water column and report a length of 0.2 s and about 100 events per minute. This spacing is closer to the here reported burst spacing in the eruption coda than the bubble collapses at depth. However, due the fast burst sequence it might also merge into a persistent background tremor if seismometers are far from the source.

Some multidisciplinary studies addressed the number of bubble traps and their depth (Ardid et al., 2019; Belousov et al., 2013; Cros et al., 2011; Munoz-Saez, Manga, et al., 2015; Munoz-Saez, Namiki, & Manga, 2015; Namiki et al., 2014; Rudolph et al., 2012; Vandemeulebrouck et al., 2013; Vandemeulebrouck et al., 2014; Wu et al., 2019). Bubble traps were commonly located at 5–40 m depth (Table 1) and in rare cases at larger depth (Namiki et al., 2014; Rudolph et al., 2012). Consistently, we inferred a bubble trap at a mean depth of 23.7 ± 4.4 m.

However, we locate it 13–23 m west of Strokkur. The tilt sensor supports this location as both tilt components exponentially increase during eruption, decrease in Phase 2 and increase in Phases 3 and 4. The sensor was therefore not oriented perfectly radial to the pressure source southwest of the geyser conduit at depth. Most publications do not resolve the relative location of the bubble trap with respect to the conduit. However, at Lone Star and Old Faithful, US the reservoir was inferred to be offset to the geyser conduit (Vandemeulebrouck et al., 2013; Vandemeulebrouck et al., 2014). Vandemeulebrouck et al. (2013) located bubble collapse signals from 10 to 15 Hz within a 20 m deep, 20 m offset bubble trap, migrating into the conduit in the recharge cycle and exponentially upwards to 10 m depth. Our depth location and lateral offset is also similar to the results of Wu et al. (2017) who located an up to 200 m wide reservoir at 10–60 m depth, 100 m southwest of Old Faithful. The conduit is vertical down to a central depth below 15 m, then bends into a horizontal conduit of 20 m length (Vandemeulebrouck et al., 2013) and followed by another vertical continuation down to more than about 80 m from the surface (Wu et al., 2019). The latter could be mapped using 1–5 Hz seismic tremor during the recharge cycle. The feeding system therefore has a constant lateral offset of 20 m to Old Faithful's conduit on the surface. Similarly, Ardid et al. (2019) modeled the seismic broadband deformation caused by El Jefe geyser, Chile and inferred a depth of 10 m and width of 6 m for the bubble trap. Here, we located the tremor using the 3–9 Hz frequency band at 5–35 m depth and interpret it as conduit system. We could not resolve a different source depth region and hence tremor source mechanism at frequencies above 10 Hz.

One bubble trap was mostly inferred (Table 1). However, Kieffer (1984) interpreted the two water levels inside the conduit of Old Faithful as two storage regions at 10–12 m and 18–22 m depth. Nishimura et al. (2006) found a correlation between eruption duration and waiting time afterward. Since the long waiting times randomly shortened without any systematic pattern, they interpreted it as two bubble chambers beneath the vent. Based on our tremor location we suggest one bubble trap feeding all eruption types at Strokkur and similar mechanisms driving single to sextuple eruptions.

6. Conclusion

We recorded the eruptive cycle of single to sextuple eruptions at Strokkur geyser with a multidisciplinary network of seismometers, pressure sensors, video cameras and one tiltmeter. The pressure, tilt and seismic sensors allowed us to further the understanding of subsurface conduit processes. These processes were linked through the water column to the surficial water changes recorded by the pressure sensors and cameras. Processes from depth unveil themselves as bubbling, thumps and slight ground shaking or even sloshing water surface and water level drops at the surface.

Here we find that all eruptive cycles consist of 4 phases: (1) eruption, (2) water refilling of the upper conduit, (3) heating and gas accumulation in the bubble trap and (4) regular bubble collapses in the conduit at depth. Gases accumulate in the bubble trap until one first bubble escapes into the conduit. Further bubbles leave this bubble trap as a trail of bubbles and burst at around 9.9 m depth. They heat the fluids in the conduit until thermodynamic conditions for an eruption are met and the bubble bursts on the surface into a water fountain for a few seconds (Figure 6). Hence, Phase 4 of the pool geyser reported here might correspond to the pre-play phase of cone geysers.

Single to sextuple eruptions have similar temporal spacings between bubble collapses in Phases 3 and 4 while the duration of the phases increases. We therefore conclude that all eruption types are fed from the same reservoir and mechanisms while more heat, gases and water are lost from the bubble trap during multi-tuple eruptions. We located this bubble trap using tremor at a mean depth of 23.7 ± 4.4 m, 13–23 m west of the conduit and hence provide documented evidence for an bubble trap beneath a pool geyser. We conclude that, although in past decades Strokkur was artificially changed by drainage and drilling, its driving system is controlled by complex natural conduit and reservoir geometries at depth.

Data Availability Statement

Seismic data of this Strokkur experiment are available through GEOFON (Eibl, Mueller, et al., 2020; Eibl, Walter, et al., 2020): https://doi.org/10.5880/GFZ.2.1.2020.007 and https://geofon.gfz-potsdam.de/doi/network/7L/2017. We used openly available Python toolboxes for the processing (Heimann et al., 2017; Megies et al., 2011).

References

Ardid, A., Vera, E., Kelly, C., Manga, M., Munoz-Saez, C., Maksymowicz, A., et al. (2019). Geometry of Geyser plumbing inferred from ground deformation. *Journal of Geophysical Research: Solid Earth*, *124*(1), 1072–1083. https://doi.org/10.1029/2018JB016454

Azzalini, A., & Bowman, A. W. (1990). A look at some data on the old faithful Geyser. *Applied Statistics*, *39*(3), 357–365. https://doi.org/10.2307/2347385

Barth, T. F. W. (1940). Geysir in Iceland. *American Journal of Science*, *238*(6), 381–407. https://doi.org/10.2475/ajs.238.6.381

Belousov, A., Belousova, M., & Nechayev, A. (2013). Video observations inside conduits of erupting geysers in Kamchatka, Russia, and their geological framework: Implications for the geyser mechanism. *Geology*, *41*(4), 387–390. https://doi.org/10.1130/G33366.1

Bopp, M. (1992). *Kombinierte Polarisations- und Arrayanalyse seismischer Daten aus dem Umfeld der Kontinentalen Tiefbohrung (Unpublished doctoral dissertation)*. Ludwig-Maximilians-Universität München

Bunsen, R. (1847). Ueber den innern Zusammenhang der pseudovulkanischen Erscheinungen Islands. *Annals of Chemistry and Pharmacy*, *62*, 1–59. https://doi.org/10.1002/jlac.18470620102

Commander, K. W., & Prosperetti, A. (1989). Linear pressure waves in bubbly liquids: Comparison between theory and experiments. *The Journal of the Acoustical Society of America*, *85*(2), 732–746. https://doi.org/10.1121/1.397599

Cros, E., Roux, P., Vandemeulebrouck, J., & Kedar, S. (2011). Locating hydrothermal acoustic sources at Old Faithful Geyser using Matched Field Processing. *Geophysical Journal International*, *187*(1), 385–393. https://doi.org/10.1111/j.1365-246X.2011.05147.x

Dawson, P. B., Benítez, M. C., Lowenstern, J. B., & Chouet, B. A. (2012). Identifying bubble collapse in a hydrothermal system using hidden Markov models. *Geophysical Research Letters*, *39*(1). https://doi.org/10.1029/2011GL049901

Descloizeaux, A. (1847). LX. Physical and geological observations on the principal Geysirs of Iceland. *The London, Edinburgh, and Dublin Philosophical Magazine and Journal of Science*, *30*(203), 391–409. https://doi.org/10.1080/14786444708645417

Eibl, E. P., Hainzl, S., Vesely, N. I. K., Walter, T. R., Jousset, P., Hersir, G. P., et al. (2020). Eruption interval monitoring at Strokkur Geyser, Iceland. *Geophysical Research Letters*, *47*.

Eibl, E. P., Jousset, P., Dahm, T., Walter, T. R., Hersir, G. P., & Vesely, N. I. K. (2019). *Seismic experiment at the Strokkur Geyser, Iceland, allows to derive a catalog of over 70,000 eruptions*. GFZ Data Services. https://doi.org/10.5880/GFZ.2.1.2019.005

Eibl, E. P. S., Mueller, D., Allahbakhshi, M., Walter, T. R., Jousset, P., Hersir, G. P., & Dahm, T. (2020). Multidisciplinary dataset at the Strokkur Geyser, Iceland, allows to study internal processes and to image a bubble trap. *GFZ Data Services*. https://doi.org/10.5880/GFZ.2.1.2020.007

Eibl, E. P. S., Walter, T., Jousset, P., Dahm, T., Allahbakhshi, M., Müller, D., & Hersir, G. (2020). 1 year seismological experiment at Strokkur in 2017/18. GFZ Data Services. Other/Seismic Network. https://doi.org/10.14470/2Y7562610816

Gouveia, F. J., & Friedmann, S. J. (2006). *Timing and prediction of CO2 eruptions from crystal Geyser, UT (Tech. Rep.)*. Lawrence Livermore National Laboratory. https://doi.org/10.2172/897988

Grant, M. A., & Sorey, M. L. (1979). The compressibility and hydraulic diffusivity of a water-steam flow. *Water Resources Research*, *15*(3). https://doi.org/10.1029/wr015i003p00684

Heimann, S., Kriegerowski, M., Isken, M., Cesca, S., Daout, S., Grigoli, F., et al. (2017). *Pyrocko - An open-source seismology toolbox and library. V. 0.3 (Tech. Rep.)*. GFZ. https://doi.org/10.5880/GFZ.2.1.2017.001

Hurwitz, S., & Shelly, D. R. (2017). Illuminating the voluminous subsurface structures of old faithful Geyser, Yellowstone National Park. *Geophysical Research Letters*, *44*(20), 10328–10331. https://doi.org/10.1002/2017GL075833

James, M. R., Lane, S. J., & Chouet, B. A. (2006). Gas slug ascent through changes in conduit diameter: Laboratory insights into a volcano-seismic source process in low-viscosity magmas. *Journal of Geophysical Research*, *111*(5). https://doi.org/10.1029/2005JB003718

Jaupart, C., & Vergniolle, S. (1988). Laboratory models of Hawaiian and Strombolian eruptions. *Nature*, *331*, 9–12. https://doi.org/10.1038/331058a0

Johnston, S., Kanamori, H., & Sturtevant, B. (1998). Bubble collapse as the source of tremor at old faithful Geyser. *Journal of Geophysical Research*, *103*(B10), 24283–24299. https://doi.org/10.1029/98JB01824

Karlstrom, L., Hurwitz, S., Sohn, R., Vandemeulebrouck, J., Murphy, F., Rudolph, M. L., et al. (2013). Eruptions at Lone Star Geyser, Yellowstone National Park, USA: 1. Energetics and eruption dynamics. *Journal of Geophysical Research: Solid Earth*, *118*(8), 4048–4062. https://doi.org/10.1002/jgrb.50251

Kedar, S., Sturtevant, B., & Kanamori, H. (1996). The origin of harmonic tremor at Old Faithful geyser. *Nature*, *379*, 708–711. https://doi.org/10.1038/379708a0

Kieffer, S. W. (1984). Seismicity at Old Faithful Geyser: An isolated source of geothermal noise and possible analogue of volcanic seismicity. *Journal of Volcanology and Geothermal Research*, *22*, 59–95. https://doi.org/10.1016/0377-0273(84)90035-0

Megies, T., Beyreuther, M., Barsch, R., Krischer, L., & Wassermann, J. (2011). ObsPy - what can it do for data centers and observatories? *Annals of Geophysics*, *54*(1), 47–58. https://doi.org/10.4401/ag-4838

Munoz-Saez, C., Manga, M., Hurwitz, S., Rudolph, M. L., Namiki, A., & Wang, C.-Y. (2015). Dynamics within geyser conduits, and sensitivity to environmental perturbations: Insights from a periodic geyser in the El Tatio geyser field, Atacama Desert, Chile. *Journal of Volcanology and Geothermal Research*, *292*, 41–55. https://doi.org/10.1016/j.jvolgeores.2015.01.002

Munoz-Saez, C., Namiki, A., & Manga, M. (2015). Geyser eruption intervals and interactions: Examples from El Tatio, Atacama, Chile. *Journal of Geophysical Research: Solid Earth*, *120*, 7490–7507. https://doi.org/10.1002/2015JB012364

Namiki, A., Muñoz-Saez, C., & Manga, M. (2014). El Cobreloa: A geyser with two distinct eruption styles. *Journal of Geophysical Research: Solid Earth*, *119*(8), 6229–6248. https://doi.org/10.1002/2014JB011009

Nishimura, T., Ichihara, M., & Ueki, S. (2006). Investigation of the Onikobe geyser, NE Japan, by observing the ground tilt and flow parameters. *Earth Planets and Space*, *58*(12), 21–24. https://doi.org/10.1186/bf03351967

Rasht-Behesht, J. S. (1965). Earth tremors generated by Old Faithful Geyser. *Science*, *150*(3695), 494–496. https://doi.org/10.1126/science.150.3695.494

Reed, M. H., Munoz-Saez, C., Hajimirza, S., Wu, S.-M., Barth, A., Girona, T., et al. (2021). The 2018 reawakening and eruption dynamics of Steamboat Geyser, the world's tallest active geyser. *Proceedings of the National Academy of Sciences of the United States of America*, *118*(2), e2020943118. https://doi.org/10.1073/pnas.2020943118

Rinehart, J. S. (1968). Seismic signatures of some Icelandic Geysers. *Journal of Geophysical Research*, *73*(14), 4609–4614. https://doi.org/10.1029/jb073i014p04609

Rudolph, M. L., Manga, M., Hurwitz, S., Johnston, M., Karlstrom, L., & Wang, C. Y. (2012). Mechanics of old faithful Geyser, Calistoga, California. *Geophysical Research Letters*, *39*(24), 1–5. https://doi.org/10.1029/2012GL054012

Soule, T. R., Jousset, P., Allahbakhshi, M., Witt, T., Gudmundsson, M. T., & Hersir, G. P. (2020). Underwater and drone based photogrammetry reveals structural control at Geysir geothermal field in Iceland. *Journal of Volcanology and Geothermal Research*, *391*, 106282. https://doi.org/10.1016/j.jvolgeores.2018.01.010

Torfason, H. (1985). The Great Geysir, (p. 23). Reykjavik: Geysir Conservation Committee.

Torfason, H. (1995). *Strokkur (in Icelandic) (Tech. Rep.)*. Reykjavik: Orkustofnun.

Vandemeulebrouck, J., Roux, P., & Cros, E. (2013). The plumbing of Old Faithful Geyser revealed by hydrothermal tremor. *Geophysical Research Letters*, *40*(10), 1989–1993. https://doi.org/10.1002/grl.50422

Vandemeulebrouck, J., Sohn, R. A., Rudolph, M. L., Hurwitz, S., Manga, M., Johnston, M. J. S., et al. (2014). Eruptions at Lone Star geyser, Yellowstone National Park, USA: 2. Constraints on subsurface dynamics. *Journal of Geophysical Research: Solid Earth*, *119*, 8688–8707. https://doi.org/10.1002/2014JB011526

Wang, C.-Y., & Manga, M. (2010). Earthquakes and Water. Earthquakes and water, lecture notes in earth sciences (Vol. 114, pp. 117–123). Springer-Verlag Berlin Heidelberg. https://doi.org/10.1007/978-3-642-00810-8_7

Wu, S. M., Lin, F. C., Farrell, J., & Allam, A. (2019). Imaging the deep subsurface plumbing of old faithful Geyser from low-frequency hydrothermal tremor migration. *Geophysical Research Letter*, *46*(13), 7315–7322. https://doi.org/10.1029/2018GL081771

Wu, S.-M., Ward, K. M., Farrell, J., Lin, F.-C., Karplus, M., & Smith, R. B. (2017). Anatomy of old faithful from subsurface seismic imaging of the yellowstone upper Geyser basin. *Geophysical Research Letters*, *44*(20), 10240–10247. https://doi.org/10.1002/2017GL075255

Zhang, J. Y., Yan, C., & Huang, X. X. (2009). Edge detection of images based on improved sobel operator and genetic algorithms. In *Proceedings of 2009 international conference on image analysis and signal processing, iasp 2009* (pp. 32–35). https://doi.org/10.1109/IASP.2009.5054605